Chemical
Science

ROYAL SOCIETY
OF CHEMISTRY

EDGE ARTICLE

View Article Online
View Journal

Check for updates

Cite this: DOI: 10.1039/d6sc00107f

All publication charges for this article have been paid for by the Royal Society of Chemistry

Solvent–temperature coupled hydride transfer controls product selectivity in the HSiR$_3$/KO^{t}Bu catalytic system

Haojiang Yao,[ab] Zhenhao Zhou,[bc] Ye Liu, *[d] Dong H. Zhang *[b] and Guohui Li *[bd]

Received 6th January 2026
Accepted 30th March 2026

DOI: 10.1039/d6sc00107f

rsc.li/chemical-science

The HSiR$_3$/KO^{t}Bu catalytic system affords a notable regioselective C–H silylation reaction using alkaline earth metals, yet its mechanistic origins and the temperature-dependent selectivity inversion remain unresolved. Here, we combine active learning neural network potentials with long-timescale *ab initio* quality molecular dynamics and enhanced sampling to simulate the HSiEt$_3$/KO^{t}Bu catalyzed deprotonation reaction of *N*-methylindole in a complete *operando* solution environment. We found that KO^{t}Bu can rapidly aggregate in organic solution to form catalyst clusters, which are able to activate and stabilize a hydride derived from silane, and this *operando* generated hydride is the catalytically active species. The hydride is able to deprotonate C2 and C3 protons on *N*-methylindole, and this reaction site selectivity is affected by the stability of the cluster controlled by solvent and temperature coupling, which gives rise to nonlinear activation entropy of the C3 pathway in the neat silane environment. Unlike tetrahydrofuran solutions, the weak polarity of neat silanes makes it difficult to support deprotonation reactions at the less acidic C3 position at high temperature, thus affecting temperature-dependent selectivity. These results provide a microscopic predictive framework for tuning the selectivity in base-promoted hydrosilane chemistry and illustrate how explicit operational solvation and cluster formation can reshape mechanistic conclusions drawn from static models.

Introduction

Heteroarylsilanes are valuable building blocks in pharmaceutical and functional molecular design, as the incorporation of silicon into heteroaromatic frameworks can enhance lipophilicity, metabolic stability, and membrane permeability.[1,2] Among available synthetic strategies, direct C–H silylation of heteroarenes represents an attractive yet fundamentally challenging transformation, owing to the low acidity and inertness of aromatic C–H bonds.[3] Conventional approaches typically rely on prefunctionalized organolithium or organomagnesium intermediates[4] or transition metal catalysts such as Ru, Rh, or Ir,[5–7] which often suffer from limited functional-group tolerance, poor sustainability, or concerns related to metal contamination.

A notable breakthrough was reported by Grubbs and coworkers, who developed an Earth-abundant metal C–H silylation protocol using potassium *tert*-butoxide (KO^{t}Bu) and hydrosilanes as the silicon source (Scheme 1a).[8] This HSiR$_3$/KO^{t}Bu system exhibits broad substrate scope, high regioselectivity, and operational simplicity and has since been extended to numerous heteroaromatic and carbocyclic substrates. Despite its synthetic utility, however, the microscopic mechanism of this catalytic system remains under active debate. Several pathways have been proposed, including electron transfer,[9–12] hydrogen atom transfer[13] and hydride transfer mechanisms (Scheme 1),[10,13–15] reflecting the mechanistic complexity of this system and its sensitivity to reaction conditions.

Particularly intriguing is the experimentally observed dependence of regioselectivity on solvent and temperature, including cases of temperature-dependent selectivity inversion.[11] Desorption electrospray ionization mass spectrometry (DESI-MS) experiments have identified transient deprotonated heteroarenes and pentacoordinate silicate species consistent with an ionic hydride-transfer pathway.[15] The origin of regioselectivity, and how it is affected by reaction conditions, has not been explained at a molecular level. In particular, it remains unclear how the solvent environment and temperature cooperatively modulate the stability of reactive intermediates and transition states in this strongly ionic system.

---

[a] *School of Chemistry and Materials Science, University of Science and Technology of China, Hefei, 230026, China*

[b] *State Key Laboratory of Chemical Reaction Dynamics, Dalian Institute of Chemical Physics, Chinese Academy of Sciences, Dalian, 116023, China. E-mail: ghli@dicp.ac.cn; zhangdh@dicp.ac.cn*

[c] *University of Chinese Academy of Sciences, Beijing 100049, China*

[d] *Interdisciplinary Research Center for Biology and Chemistry, Liaoning Normal University, Dalian, 116029, China. E-mail: yeliu@lnnu.edu.cn*

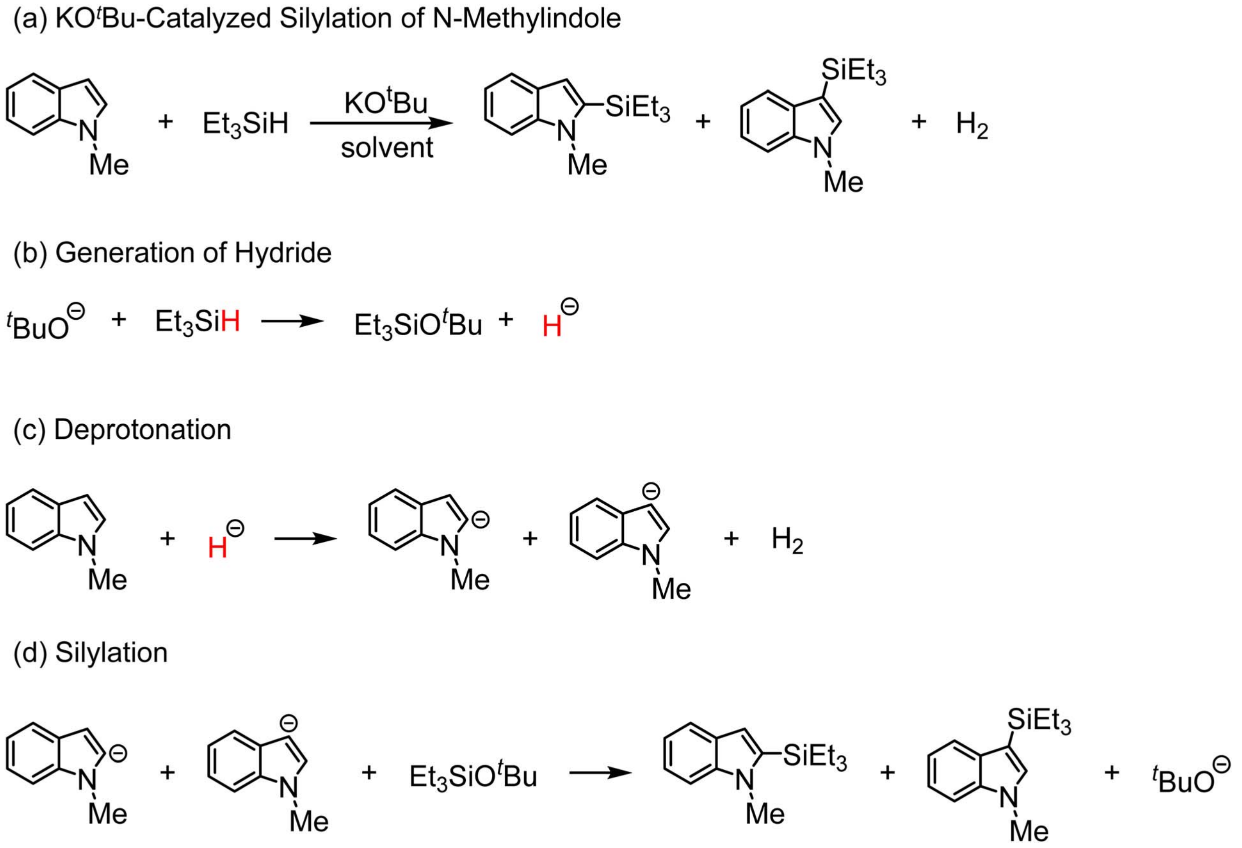

Scheme 1 (a) KO^{t}Bu-catalyzed *N*-methylindole silylation reaction. (b–d) The proposed catalytic reaction mechanistic steps using simplified and intuitive reaction equations to describe the catalytic process.

From a theoretical perspective, most mechanistic studies of the HSiR$_3$/KO^{t}Bu system have relied on static quantum chemical calculations, often employing implicit solvent models or small, predefined coordination clusters. While these approaches can provide qualitative insights, they inherently neglect the dynamic formation of multimeric catalytic species and the fluctuating solvation structures present under *operando* conditions.[16] This limitation becomes especially severe when charged intermediates or hydride species[17,18] are involved, as static models fail to capture localized polarization, nonlinear dielectric responses,[19] and temperature-dependent entropic effects.[20] As a result, key experimental phenomena, such as solvent-specific reactivity trends and the nontrivial temperature dependence of selectivity, remain inaccessible to conventional static models.

Here, we address these challenges by employing *ab initio* quality machine learning molecular dynamics (MLMD) simulations combined with an active-learning workflow to investigate the HSiR$_3$/KO^{t}Bu catalytic system under realistic solution-phase conditions. This fully dynamic approach enables explicit treatment of solvent molecules, *operando* formation of multimeric KO^{t}Bu clusters, and temperature-dependent structural fluctuations, without imposing preconceived mechanistic assumptions. Crucially, this workflow extends mechanistic studies of solution-phase reactions beyond static, few-molecule models to simulations of chemically realistic, many-body environments, allowing direct modeling of *operando* experimental conditions at *ab initio* accuracy.

By systematically comparing tetrahydrofuran (THF) solvent and neat silane environments over a broad temperature range, we uncover how solvent–temperature coupling governs hydride generation, free energy of deprotonation, and ultimately product selectivity. Our results provide a microscopic and thermodynamic framework that rationalizes experimentally observed selectivity patterns and their temperature-dependent inversion, establishing dynamic hydride transfer as the key mechanistic origin of catalysis in this system.

Methods

Neural network potential

The complete code used to construct the neural network potential (NNP) was implemented using the DeePMD-kit package.[21] The Deep Potential Smooth Edition (DeepPot-SE)[22] model was employed for training (Fig. 1a). This model consists of two neural networks: an embedding network and a fitting network, both adopting a residual neural network (ResNet) architecture. The layer sizes of the embedding network were set to (25, 50, 100), with an embedding matrix size of 12. The fitting network consisted of three hidden layers with 240 nodes each, *i.e.*, (240, 240, 240). The cutoff radius was set to 6.0 Å, and the descriptors were smoothly decayed from 0.5 Å to 6.0 Å. The

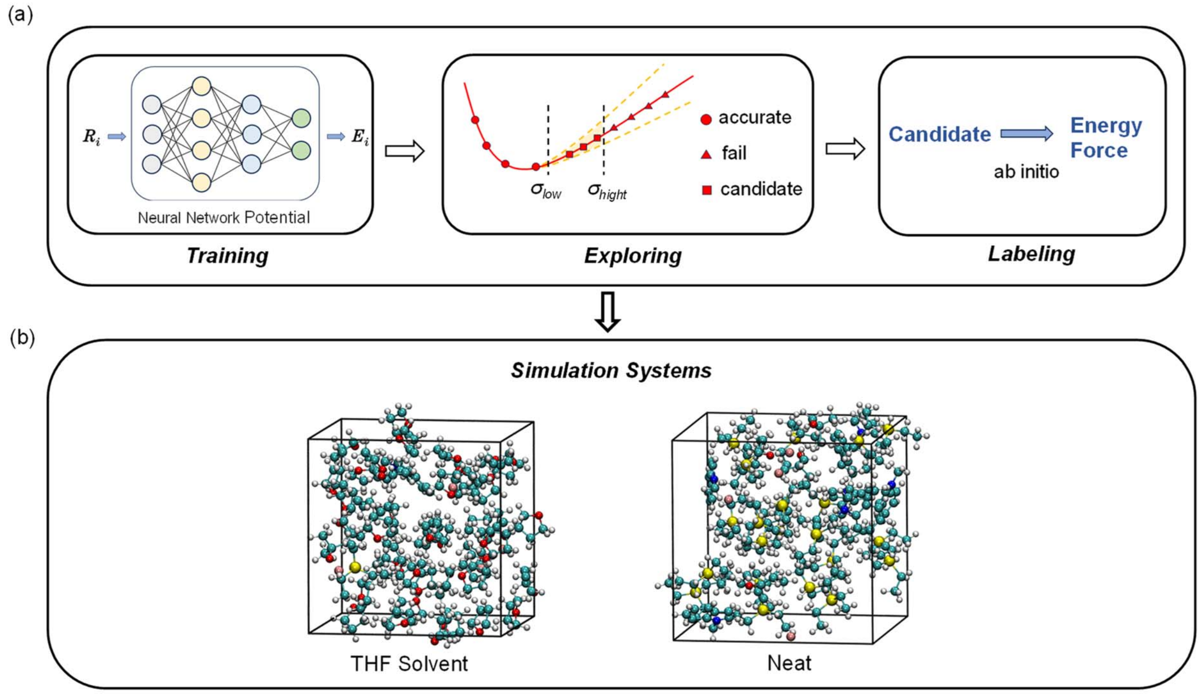

Fig. 1 (a) Active learning for neural network potential training and chemical space exploration workflow. (b) Boxes constructed to simulate catalytic reactions in real solvent environments.

learning rate was initially set to 1.0×10^{-3} and decayed to 3.51×10^{-8} over the course of training. As the training set expanded, the number of training steps increased accordingly, and the final model was trained for 2 200 000 steps, covering approximately 150 000 conformations.

MLMD

We created two models based on the feeding ratios used in the experiment (Fig. 1b).[8,11] In the THF solvent system, a periodic cubic box at 300 K contains 4 KO^{t}Bu, 1 triethylsilane (Et_3SiH), 1 *N*-methylindole, and 40 THF molecules (Table S1, Box 1, 622 atoms in total). In the neat silane system, the box contains 4 KO^{t}Bu, 21 Et_3SiH, and 7 *N*-methylindole molecules (Table S1, Box 2, 676 atoms in total). The catalyst in both systems is KO^{t}Bu, and the reactants are Et_3SiH and *N*-methylindole (Fig. S1). Additionally, simulations were extended to examine the aggregation patterns of KO^{t}Bu catalysts at finer concentrations. Detailed simulation specifications are provided in Table S1. All simulations were performed in the *NPT* ensemble at a temperature of 300–450 K. The *NPT* ensemble was temperature controlled using a Nose–Hoover thermostat[23] and pressure controlled using a Parrinello–Rahman barostat,[24] with the time step set to 0.5 fs and the temperature and stress damping parameters set to 50 fs and 500 fs, respectively. The pressure is set to 1 bar. Enhanced sampling was enabled through PLUMED,[25] which was activated during biased simulations.

We employed the well-tempered metadynamics (WT-MetaD) method,[26] which is an enhanced-sampling technique used in MD to efficiently explore free-energy landscapes and accelerate rare events. In WT-MetaD, a history-dependent bias potential is added along selected collective variables (CVs) to encourage the system to escape free-energy minima. A Gaussian bias $V(s,t)$ is added in CV space:w

$$V(s,t) = \sum_{t'<t} \omega\left(t'\right) \exp\left[-\frac{\left(s - s\left(t'\right)\right)^2}{2\sigma^2}\right]$$

here s is the collective variable, σ is the Gaussian width and $\omega(t)$ is the time-dependent height of the Gaussian. The hill height decays asw

$$\omega(t) = \omega_0 \exp\left[-\frac{V(s(t),t)}{k_B \Delta T}\right]$$

here ω_0 is the initial hill height and ΔT is the fictious bias temperature. The free energy is obtained as

$$F(s) = -\frac{T + \Delta T}{\Delta T} V(s)$$

An equalized metadynamics bias is applied along the CV to increase the probability of molecular collisions leading to a reaction. The advantage of temperature-controlled metadynamics is that it limits the size of the deposition bias, prevents the exploration of unphysical regions of the reaction space, and allows for accurate calculation of the free energy.[27] Free energy curves calculated using WT-MetaD are verified for convergence (Fig. S3 and S4).

Workflow

Our active learning workflow aims to build an accurate neural network potential and explore chemical reactivity with minimal computational cost and chemical intuition (Fig. 1a). This strategy is efficient, generalizable, and automated. Based on the bias calculation method proposed by Zhang *et al.*,[28] we use multiple NNP models (initialized with different random seeds) to evaluate the force uncertainty of the whole system. The maximum deviation in atomic forces, denoted as σ^f, is used to select new data points:wh

$$\sigma^{\mathrm{f}} = \max_{\mathrm{i}} \sqrt{\frac{1}{4} \sum_{\alpha=1}^{4} \left\| F_{\mathrm{i}}^{\alpha} - \overline{F}_{\mathrm{i}} \right\|^2}$$

ere 1/4 corresponds to the use of four NNPs. $\bar{F}_{\mathrm{i}}$ is the averaged force on atom i from the four models, and F_{i}^{α} is the predicted force on atom i from model α. Two thresholds were set for labeling: $\sigma_{\mathrm{low}}^{\mathrm{f}} = 0.20$ eV Å^{-1} and $\sigma_{\mathrm{high}}^{\mathrm{f}} = 0.35$ eV Å^{-1}. For each exploration iteration, the average model deviation $\sigma_{\mathrm{avg}}^{\mathrm{f}}$ was calculated. Conformations with σ^{f} values between ($\sigma_{\mathrm{low}}^{\mathrm{f}}$ + $\sigma_{\mathrm{avg}}^{\mathrm{f}}$) and ($\sigma_{\mathrm{high}}^{\mathrm{f}}$ + $\sigma_{\mathrm{avg}}^{\mathrm{f}}$) were considered informative and were selected for labeling *via* DFT calculations and then added to the training set. Structures with σ below the lower bound were regarded as accurately described, while those exceeding the upper bound were discarded as unphysical. This iterative workflow, combining NNP training with WT-MetaD, was repeated until the training dataset was sufficiently comprehensive (Fig. S2).

DFT calculations

All density functional theory (DFT) calculations were performed using the freely available CP2K/QUICKSTEP package.[29] The total energies and atomic forces in the dataset were computed at the same theoretical level as that used for the *ab initio* molecular dynamics (AIMD) simulations, ensuring internal consistency. Electronic structure calculations employed the Perdew–Burke–Ernzerhof (PBE) exchange–correlation functional,[30] in conjunction with Goedecker–Teter–Hutter (GTH) pseudopotentials[31,32] to describe the core electrons. We used the DZVP-MOLOPT-PBE-GTH basis set (a double ζ valence basis set with polarization) optimized for the PBE functional. The plane-wave cutoff for the finest integration grid was set to 400 Ry. Grimme's DFT-D3 dispersion correction[33] was applied to account for long-range van der Waals interactions and the orbital transform (OT) algorithm[34] was used to optimize the self-consistent wave function (SCF). The choice of the PBE functional with Grimme's D3 dispersion correction (PBE-D3) reflects a balance between computational efficiency and reliability, and its robust and transferable performance makes it particularly suitable for constructing NNPs that capture reactive dynamics in complex solution phases.[35–37]

Results

Operando formation of catalytic clusters and generation of hydride

To facilitate the discussion of the reaction mechanism, the catalytic silylation of *N*-methylindole by the $\mathrm{HSiEt_3/KO}^t\mathrm{Bu}$ system can be divided into three stages: hydride generation (Scheme 1b), deprotonation (Scheme 1c), and silylation (Scheme 1d).

The formation of a free hydride species in solution is exceptionally rare and mechanistically intriguing. Its microscopic pathway is often ambiguous because a hydride can only exist when a catalyst provides a strongly electrostatic and highly stabilizing environment, typically through *operando* formed clusters.[38–40]

In the first stage of the reaction, we defined a collective variable (CV) based on the $\mathrm{KO}^t\mathrm{Bu}$-$\mathrm{HSiEt_3}$ distance to monitor their mutual approach and subsequent bond rearrangement.

In the initial THF environment simulation box, $\mathrm{KO}^t\mathrm{Bu}$ ion pairs were placed in a dispersed configuration (Fig. 2). As the simulation progressed, $\mathrm{KO}^t\mathrm{Bu}$ gradually organized into stable clusters.

The time-resolved MLMD trajectory clearly shows the aggregation process: a dimer appears in the first 20 ps, followed by the formation of a trimer at around 100 ps. After a lot more time has passed, a tetramer (the primary clusters capable of forming hydrides) appears for the first time around 2 ns.

To place the simulated potassium alkoxide aggregate in structural context, it is useful to compare it with representative single-crystal potassium alkoxide structures. Chisholm *et al.*[41] showed that $\mathrm{KO}^t\mathrm{Bu}$ can be isolated as a cubane-like tetramer $[\mathrm{KO}^t\mathrm{Bu}]_4$, while crystallization from $^t\mathrm{BuOH}$-containing media affords the hydrogen-bonded ribbon-chain precursor

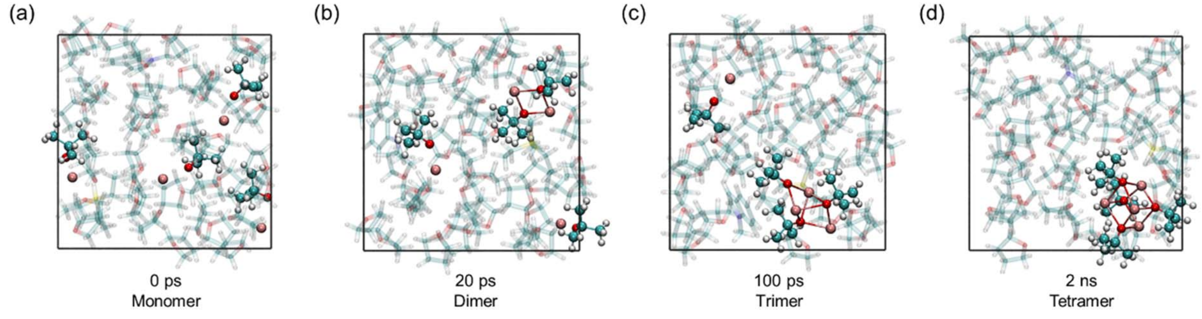

Fig. 2 (a–d) Sequential snapshots at 0 ps, 20 ps, 100 ps, and 2 ns, highlighting the evolution of $\mathrm{KO}^t\mathrm{Bu}$ molecules; other molecules are rendered transparent.

$[KO^tBu\cdot{}^tBuOH]_n$. Under strongly donor-stabilizing conditions, lower-order species such as elemental [K(18-crown-6)(O^{t}Bu)] can be obtained, where crown ether coordination saturates the potassium center.[42] It can thus be seen that in weakly polar solvents, potassium alkoxides tend to adopt self-aggregation structures. Therefore, when considering potassium alkoxide catalysts, it is recommended to treat aggregates as the fundamental structural units.

In our simulations, the radial distribution function (RDF) between K^+ and the oxygen atom of THF in the system exhibits a first coordination shell peak at $r = 2.85$ Å (Fig. S5a), with an average coordination number CN = 3.2 for K^+ in THF (Fig. S5b). These values are in close agreement with results obtained from similar THF-solvated potassium complex crystals.[43,44]

We conduct additional simulations with larger and more dilute boxes that more closely approximate experimental composition regimes (Table S1). In these extended systems, tetrameric KO^{t}Bu aggregates persist as the dominant and enduring catalytic units throughout molecular dynamics simulations even as collision frequencies decrease (Fig. S6). This indicates that tetramer formation does not solely result from simulation bias originating from the initial high-density setup.

Because KO^{t}Bu self-aggregation and complexation of KO^{t}Bu with silane constitute competing processes (Fig. S7), these trajectories directly establish that aggregation is the dominant pathway, leading to the *operando* formation of tetrameric KO^{t}Bu clusters that serve as the key reactive units.

Importantly, the formation of the tetramer does not merely “collect” ions; it qualitatively reshapes the reactive coordination chemistry by enabling the ^{t}BuO$^-$ anion to dynamically interconvert between two coordination motifs: the tetrameric KO^{t}Bu cluster and a pentacoordinate silicon intermediate formed upon interaction with Et_3SiH (Fig. 3a and S8b). Pentacoordinate and, more generally, hypercoordinate silicon species are well precedented in the literature and have been structurally characterized in a variety of settings.[45] These include silicon hydride-containing hypervalent species and hydridosilicates.[46–48] In our case, the optimized pentacoordinate silicon adopts a distorted trigonal-bipyramidal arrangement (Fig. S8b), with an elongated axial Si–O bond of 2.03 Å, a trans Si–C bond of 2.01 Å, and two shorter equatorial Si–C bonds of 1.91 and 1.92 Å. The Si–H bond length increased from 1.50 to 1.52 Å upon activation (Fig. S8a).

Hydride generation occurs only when the pentacoordinate silicon approaches the highly charged pocket of the tetramer (Fig. 3a and b). In this configuration, the catalytic cluster establishes an intense electrostatic field and a locally polarized electrostatic environment, which collectively weaken the Si–H bond and lower the rearrangement barrier.[50,51] Once the Si–H bond undergoes heterolytic cleavage, the nascent hydride is immediately captured by the cluster core, preventing its diffusion into bulk solution. This cluster-assisted Si–H activation is inaccessible in monomeric KO^{t}Bu (Fig. S9).

Long-timescale MLMD simulations further confirm that the resulting hydride-bound cluster is kinetically stable. This observation is consistent with experimental intuition: the hydride is an extremely hard base with an exceptionally high charge density, and it cannot exist as a freely solvated species in an organic solution. Instead, it remains sequestered within a tightly multimeric cluster immediately following the cleavage of the Si–H bond.[52–54]

With this cluster-enabled mechanism established, we next quantify how the solvent environment modulates the same hydride-generation event. The free energy barriers for hydride generation differ slightly under the two examined conditions (Fig. 3c). In THF, the TS appears at 18.6 kcal mol^{-1}, whereas in the neat environment, the TS increases to 21.5 kcal mol^{-1}. Although the barrier is higher in the neat environment, both values fall within the range accessible at ambient temperatures for organic reactions. After crossing the TS, the reaction reaches the FS shown in Fig. 3b, in which a hydride is captured by the KO^{t}Bu catalyst cluster.

The charge evolution along the reaction coordinate further highlights the differentiated electrostatic environments created by THF and neat silane (Fig. 3d). In THF, the reacting hydrogen consistently carries a more negative partial charge, from the initial state to the transition state and finally to the hydride-rich product state. This indicates that the polar solvent effectively stabilises the progressive charge separation associated with Si–H heterolysis. The enhanced stabilization is most evident in the product region, where the hydride reaches a substantially more negative charge in THF, reflecting the combined effect of solvent polarity and the well-organised tetrameric potassium

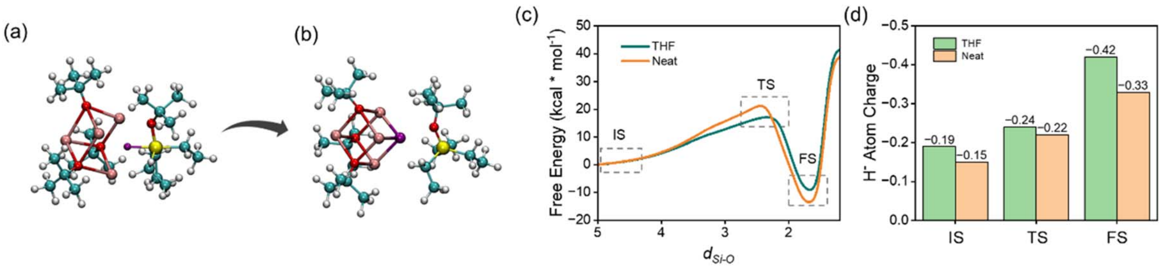

Fig. 3 (a and b) Representative snapshots of the hydride-formation transition state (TS), *i.e.*, hydride transfer and Si–H cleavage from the pentacoordinate silicon, and the corresponding final state (FS). (c) Free energy curves for hydride generation at 300 K under different solvent environments, with IS, TS, and FS labelled. (d) Atomic charges[49] of the hydride-origin hydrogen atom at IS, TS, and FS. The coloring of the atoms in all snapshots: C—cyan, H—white, O—red, Si—yellow, K—pink, and H$^-$—purple.

cluster. Conversely, the neat silane medium provides weaker dielectric screening; the hydrogen remains less negatively charged at every stage, revealing a reduced ability to accommodate charge redistribution during bond cleavage. This result also implies a difference in the free energy barrier for the deprotonation step under the two environments.

At the same time, the limited stability in a nonpolar environment explains the higher and more temperature-sensitive free energy barriers observed in neat silane. From a mechanistic perspective, THF readily supports hydride polarization through solvation, whereas neat silane relies heavily on the integrity of the multimeric KO^{t}Bu cluster to compensate for their weak solvating ability, which makes the reaction pathway more susceptible to thermal disruption of the cluster structure (see below).

Free energy of deprotonation calculation by dynamic simulation

The deprotonation reaction of *N*-methylindole constitutes the second and rate-determining stage of the catalytic cycle. This step proceeds *via* hydride-mediated abstraction of a proton from either the C2 or C3 position of the indole ring, thereby generating the reactive nucleophilic intermediates required for subsequent heterocycle silylation (Fig. 4).

The reaction is characterized by a highly ordered transition state in which the hydride nucleophile approaches the C–H bond while the surrounding solvent molecules reorganize to stabilize the charge separation being formed. As a result, the process is entropically disfavored, and its free energy barrier exhibits a pronounced temperature dependence.

To capture these effects, we performed more than 10 ns of well-tempered metadynamics simulations for each solvent environment (THF and neat silane) and temperature (300–450 K); the extended thermal range enables a systematic decomposition of temperature dependence, solvation structure, and entropy contributions.

The simulations reveal a clear and physically intuitive trend: the free energy barriers for both C2 and C3 deprotonation increase monotonically with temperature. This increase reflects the entropic penalty associated with the formation of a tightly organized transition state, where hydride binding, K^+ coordination, and solvent reorganization reduce configurational freedom.

Specifically, under THF dissolution conditions, moderate polarity and modest dielectric shielding are more effective in stabilizing the progressive charge redistribution that accompanies deprotonation from the IS (Fig. 4a) to the TS (Fig. 4b and c) than in the weakly polarized neat silane environment; as a consequence, THF yields overall lower computed free-energy barriers and a near-linear temperature dependence of $\Delta G^{\neq}$. At 300 K the calculated $\Delta G^{\neq}$ values for C2 and C3 deprotonation are 18.1 and 21.3 kcal mol^{-1}, respectively; by 450 K these barriers increase to 22.0 and 22.8 kcal mol^{-1}, reducing the intrinsic kinetic gap between the two sites (Fig. 5a). We emphasise that activation entropies drive this temperature dependence: the activation entropy is obtained from the temperature derivative of the barrier, and in THF the C2 pathway incurs a substantially larger entropy loss ($\Delta S^{\neq} = -25.7$ cal mol^{-1} K^{-1}) than the C3 pathway ($\Delta S^{\neq} = -9.8$ cal mol^{-1} K^{-1}) (Fig. 5c). The larger negative $\Delta S^{\neq}$ for C2 causes its barrier to rise more rapidly with temperature, which explains why the kinetic preference for C2 diminishes as T increases in THF.

By contrast, in the neat silane environment, the C3 pathway exhibits a pronounced, non-linear entropic response: between 300 and 350 K, the C3 barrier rises sharply (21.5 to 24.6 kcal mol^{-1}), while the C2 barrier changes only modestly (18.6 to 19.8 kcal mol^{-1}) (Fig. 5d). Structural analysis indicates that this behaviour arises from temperature-sensitive disruption of the multimeric K-hydride aggregation that particularly stabilises the ordered TS required for C3 deprotonation (Fig. 6). The abrupt change in cluster stability produces a large, non-linear change in the effective $\Delta S^{\neq}$ for C3 (Fig. 5d), which is not captured by implicit-solvent or static calculations.

We also note two important caveats relevant to experimental selectivity. First, our computed $\Delta G^{\neq}$ values do not show a strict barrier crossover within the simulated temperature range; rather, they converge, such that kinetic discrimination is reduced at high temperature in THF. Second, the final product distribution observed experimentally depends not only on these deprotonation barriers but also on the relative thermodynamic stability of the silylated products and specialized reverse reaction mechanisms different from forward reactions. Some experiments report product interconversion and small amounts

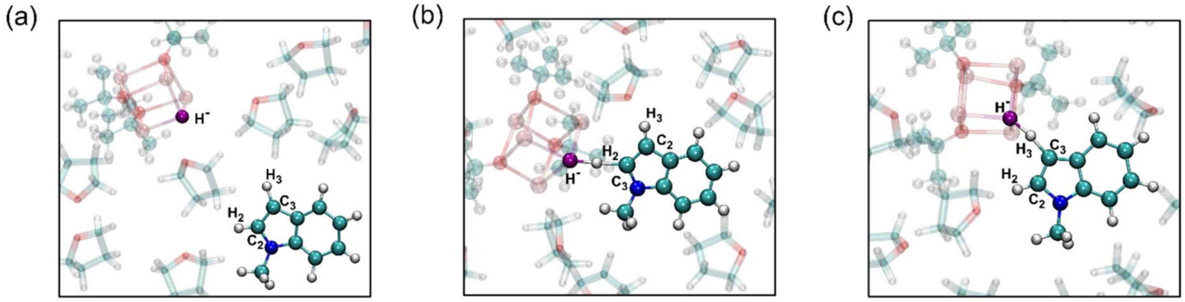

Fig. 4 Snapshots of *N*-methylindole deprotonation reactions taken from simulation trajectories. (a) IS and (b) TS of the deprotonation reaction at the C2 site. (c) C3 site deprotonation reaction. Highlighted rendering of the hydride (purple coloring) and *N*-methylindole and transparent rendering of the other species.

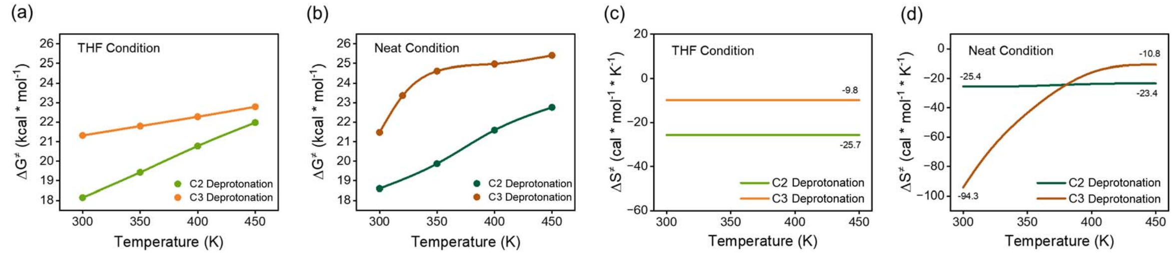

Fig. 5 (a and b) Free energy barriers ($\Delta G^{\neq}$) for C2 and C3 deprotonation as a function of temperature in the THF and neat environments. (c and d) The activation entropy ($\Delta S^{\neq}$) of the C2 and C3 deprotonation as a function of temperature in the THF and neat environments.

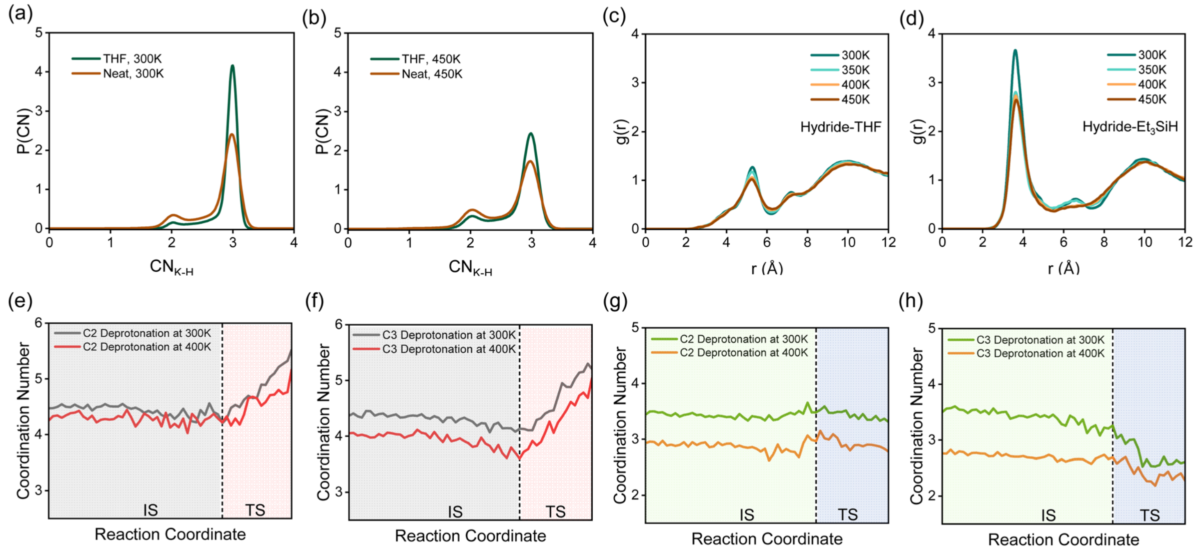

Fig. 6 (a and b) Statistics of the probability densities of the coordination number of the hydride with the surrounding potassium ions for the C3-site deprotonation reaction at 300 K and 450 K during the IS and TS periods. (c and d) Radial distribution functions of hydrides in the C3-site deprotonation reaction with THF and silane solvent molecules in the IS and TS phases at 300 K–450 K. (e and f) Coordination number of hydrides with THF solvent molecules at IS and TS during deprotonation of C2 and C3. (g and h) Coordination number of hydrides with silane solvent molecules at IS and TS states during deprotonation of C2 and C3.

of reversion to *N*-indole, and such long-timescale, multi-step processes are difficult to sample exhaustively in finite MD trajectories. For these reasons, we present the deprotonation free-energy barriers primarily as mechanistic indicators of trends (entropic sensitivity, solvent coupling, and cluster-dependence) rather than as definitive predictors of absolute product ratios. Taken together, the computed entropic trends rationalise why C3 silylation becomes increasingly competitive at elevated temperature in THF, while the strong, non-linear entropic penalty in neat silane disfavors C3 across the accessible temperature range.

These findings are consistent with the experimentally observed trends: in THF solution, the reaction predominantly affords the C2-silylated product at low temperature, but the selectivity reverses at elevated temperature, favoring the C3-silylated product.[11] In contrast, in a neat environment, C2 selectivity persists across all temperatures, and no inversion is observed.

For completeness, our NNP has been extended to silylation reactions and simulates the third step of the catalytic sequence, namely the silylation of the deprotonated indole intermediate (Fig. S10). Potassium does not play a direct mechanistic role in the final C–Si bond-forming event. Instead, the reactivity of this step is determined primarily by the position of the reactive carbon center generated in the preceding deprotonation step. Thus, the silylation process follows the regioselectivity already established upstream, rather than introducing a new potassium-controlled selectivity element.

Nonlinear entropy effects and the origin of catalytic selectivity

In conventional quantum chemical calculations employing implicit solvent models, the solvent is described as a continuum. This approximation neglects the discrete arrangement and dynamic reorganization of solvent molecules, and as a result, the entropy term in such frameworks is typically treated as temperature-independent. This means that the free energy barriers become a strictly linear function of temperature, showing a standard linear entropic effect. Therefore, the strong nonlinearity in $\Delta G^{\neq}$ observed here cannot be captured by static implicit-solvent quantum chemistry. This underlines the importance of explicit solvent dynamics and temperature-dependent structural fluctuations, which are naturally included in our MLMD simulations.

To rationalize the observed nonlinear entropic effects and site-selectivity inversion, we analyzed the structural statistics of the hydride cluster extracted from the MLMD trajectories. Throughout the reaction, from the initial state to the transition state and until H_2 is formed, the reactive hydride is tightly stabilized by cooperative ion pairing among ${}^{t}BuO^{-}$, K^{+} and H^{-}. The extent of this aggregation can be quantitatively described using the K–H coordination number. In THF, the hydrides preferentially adopt a tetrameric arrangement (coordination number = 3), with a lower probability density of trimers (Fig. 6a). In the neat silane environment, although tetramers are still the dominant polymer species, the distribution is more moderate and the probability density of trimers is elevated (Fig. 6a).

The probability of forming well-ordered tetramers decreases systematically with increasing temperature, and the distribution of tetramers and trimers becomes gentler (Fig. 6b). This change reflects enhanced thermal motions and weakened ionic associations at higher temperatures, which destabilize the synergistic stabilization provided by multiple potassium cations. Importantly, no conformations corresponding to "2K-H", "1K-H", or uncoordinated hydride species were observed, even at 450 K. The results of this study are summarized below.

Differences in aggregation states in THF and in neat silane provide a mechanistic origin for the different temperature dependences of the C2 and C3 deprotonation barriers. This can be seen in the RDFs between the hydride and solvent molecules. In THF, the structural environment of the hydride does not change significantly when the temperature increases from 300 K to 450 K. The solvent environment does not undergo rearrangement within this temperature range (Fig. 6c). This stable aggregation leads to nearly linear $\Delta G^{\neq}$ behavior for both C2 and C3 positions.

In the neat environment, from 300 K to 350 K, the solubility of the hydride decreases considerably and the stability decreases abruptly (Fig. 6d). Deprotonation of C3 is more sensitive to partial disruption of ionic clusters, as it requires a more ordered transition state and tighter hydride polymerization than C2. Loss of ion cluster integrity disproportionately destabilizes the C3 transition state, producing the nonlinear steep increase in $\Delta G^{\neq}$ observed only for the C3 pathway (Fig. 5b). Importantly, this drop is not driven by intrinsic solvent structural changes: the solvent–solvent RDFs for THF and silane show only mild, uniform temperature broadening (Fig. S11).

The electronic environments of the C2 and C3 sites are fundamentally different: whereas the enhanced acidity of the C2–H bond in *N*-methylindoles arises from the excellent resonance stability of the resulting carbanion, in which the negative charge is efficiently dispersed across the indole framework and partially transferred to the nitrogen atom, deprotonation of C3 leads to a more localized anion with reduced stability.[55]

Therefore, deprotonation at C3 is expected to require more efficient solvent stabilization. More generally, explicit solvation and solvent reorganization can play a decisive role in solution-phase ionic reaction pathways and in the associated free energy barriers.[56,57] We further quantified the solvent contributions by tracking the coordination number between the reactive hydride and solvent molecules along the reaction coordinate (Fig. 6e–h). Two representative temperatures, 300 and 400 K, were chosen to reflect typical experimental conditions.

These statistical trends reveal different solvent recombination behaviors at the two reaction sites. The significant increase in the coordination of C2 and C3 upon deprotonation in THF (Fig. 6e and f) suggests that the additional THF molecules effectively stabilize the charged species formed in TS. In a neat environment, the deprotonation of C2 and C3 showed opposite trends. The deprotonation of C2 was essentially insensitive to the silane solvent, and the coordination number of the hydride at the reaction center to silane remained almost the same with the progress of the reaction (Fig. 6g), suggesting that the solvent's ability to stabilize the charge-transfer product at this position was constant, and there was no solvent recombination. In contrast, the coordination number of silane decreases during C3 deprotonation (Fig. 6h), internal interactions dominate in the TS, and solvent molecules with weaker interactions are displaced. The ability of the solvent to stabilize the transition state of the C3 deprotonation reaction decreases, leading to an anomalous entropic effect on the free energy barriers of the reaction.

Relatively speaking, the temperature increase has a slightly greater effect on the neat environment (Fig. 6e–h), which is consistent with the previously calculated trend of a more significant change in the neat deprotonation free energy barrier with temperature.

Discussion

Whenever a new catalytic reaction is discovered, the study of its catalytic mechanism is usually the most difficult step. The $HSiR_3/KO^{t}Bu$ system is a fascinating example of organosilicon catalysis, for which multiple mechanistic pathways have been proposed, including hydride transfer, electron transfer and hydrogen atom transfer. Building upon the mechanistic framework originally advanced by Shibdas Banerjee and coworkers,[15] our work refines and extends this understanding by introducing an explicitly dynamic perspective.

For the first time, we constructed a model very close to the experimental environment and accomplished the simulation of the $HSiR_3/KO^{t}Bu$ catalytic system with the help of a neural network potential. Our results strongly support the reaction mechanism of hydride transfer, and by means of this reaction mechanism, we discuss the selectivity of the deprotonation process of de-C–H bonds under different experimental conditions. Our trend studies and analyses strongly suggest a microscopic mechanism of selectivity reversal and disappearance of selectivity reversal, which is in accordance with the experimental results and shows the correctness of our hydride transfer mechanism.

From the perspective of the tetramer $KO^{t}Bu$ catalytic reaction, if the catalytic mechanism in solution proceeds through stepwise transformations involving hydride intermediates, the system must be capable of maintaining a structurally confined and electrostatically stabilized space for the hydride to persist.

Related potassium-based catalytic systems provide useful comparisons. For example, potassium graphite (KC8) possesses a layered intercalation structure, in which potassium atoms are periodically inserted between graphene sheets.[58] In such materials, potassium atoms occupy well-defined positions within the carbon lattice, which can generate localized electrostatic environments and potential trapping sites for hydride-like species formed under reaction conditions.[59,60] Experimental studies have shown that KC8 can catalyze the same transformation,[61,62] albeit with lower activity and turnover frequency compared to KO^tBu.[11] The confined interlayer regions of KC8 may therefore provide transient stabilization sites for reactive hydride species within the carbon matrix.

Potassium hydride (KH) represents another relevant reference system. In contrast to molecular or oligomeric potassium alkoxides, KH exists as an extended ionic solid adopting a NaCl-type lattice, where hydride ions are octahedrally coordinated by six potassium cations.[63] In addition, KH is essentially insoluble in common organic solvents such as THF, meaning that reactions typically occur at the solid–liquid interface rather than through discrete solvated hydride species.[64,65] Palumbo *et al.* proposed that the active catalyst for potassium-based catalytic silylation reactions is not KO^tBu, but rather the *operando* formed KH. This form differs from commercially available solid aggregates of KH and exhibits higher reactivity.[14]

While our machine learning molecular dynamics simulations, enabled by an active learning workflow, allow for large-scale modeling of reactive systems, extending the neural network potential to additional catalytic environments still incurs considerable computational cost. This lies beyond the present scope of discussion. Nevertheless, we plan to expand our simulation dataset in future work to explore how other alkali metal based catalysts modulate hydride reactivity and stability, thereby providing a broader mechanistic framework for base-promoted silane transformations.

Conclusion

By combining machine learning molecular dynamics with active learning workflows, we capture temperature-dependent behaviors, solvent effects, and catalyst aggregation that are not possible with static quantum chemical methods. The results show that in the $HSiR_3/KO^tBu$ catalytic system, hydride formation and transfer depend on the *operando* formation of multimeric KO^tBu clusters, and the constraints of the catalytic clusters allow for sufficient lifetimes of hydrides to participate in the subsequent reactions. Second, the experimentally observed temperature-dependent selective inversion is caused by entropic effects arising from the coupling of solvent and temperature. In the neat silane environment, deprotonation of C3 requires a more organized and charge-stabilized environment than that of C2, despite its lower intrinsic acidity, and is therefore disproportionately sensitive to solvent polarity and thermal conditions. As temperature rises in weakly polar neat silane, disruption of the local solvation/cluster organization reduces transition-state stabilization for the C3 pathway, producing the observed non-linear entropic penalty and the abrupt increase in its effective free-energy barrier. This selectively suppresses the formation of the C3-derived product relative to C2 and thereby eliminates the temperature-driven selectivity reversal seen in THF. Overall, our *operando* MLMD framework bridges static mechanistic pictures and realistic condensed-phase reaction environments, providing a thermodynamic and microscopic basis for how experimental conditions modulate hydride generation/transfer and, ultimately, regioselectivity.

Author contributions

L. G. conceived and designed the research. H. Y. performed the calculations, plotted the figures and prepared the original draft. Z. Z. directed the calculations. H. Y., Y. L., and L. G. revised the manuscript. Y. L., D. Z., and L. G. supervised the research. All authors discussed and commented on the manuscript.

Conflicts of interest

The authors declare no competing financial interests.

Data availability

Supplementary information (SI): details of the simulation system; collective variables (CVs); free energy convergence; model accuracy; and additional simulation results. See DOI: https://doi.org/10.1039/d6sc00107f.

Acknowledgements

This work was supported by the LiaoNing Revitalization Talents Program (XLYC2402023 to G. L.).

References

1 J.-L. Panayides, D. L. Riley, F. Hasenmaile and W. A. L. van Otterlo, The role of silicon in drug discovery: a review, *RSC Med. Chem.*, 2024, **15**, 3286–3344.
2 K. Yamada, A. Deb, V. M. Shoba, D. Lim, B. Maji, A. E. Modell and A. Choudhary, Rational Design of Silicon-Based Zinc Ionophores, *Angew. Chem., Int. Ed.*, 2022, **61**, e202201698.
3 J. H. Docherty, T. M. Lister, G. McArthur, M. T. Findlay, P. Domingo-Legarda, J. Kenyon, S. Choudhary and I. Larrosa, Transition-Metal-Catalyzed C–H Bond Activation for the Formation of C–C Bonds in Complex Molecules, *Chem. Rev.*, 2023, **123**, 7692–7760.
4 M. C. Whisler, S. MacNeil, V. Snieckus and P. Beak, Beyond Thermodynamic Acidity: A Perspective on the Complex-Induced Proximity Effect (CIPE) in Deprotonation Reactions, *Angew. Chem., Int. Ed.*, 2004, **43**, 2206–2225.
5 I. V. Seregin and V. Gevorgyan, Direct transition metal-catalyzed functionalization of heteroaromatic compounds, *Chem. Soc. Rev.*, 2007, **36**, 1173–1193.

6 C. Cheng and J. F. Hartwig, Rhodium-Catalyzed Intermolecular C–H Silylation of Arenes with High Steric Regiocontrol, *Science*, 2014, **343**, 853–857.

7 B. Lu and J. R. Falck, Efficient Iridium-Catalyzed C═H Functionalization/Silylation of Heteroarenes, *Angew. Chem., Int. Ed.*, 2008, **47**, 7508–7510.

8 A. A. Toutov, W.-B. Liu, K. N. Betz, A. Fedorov, B. M. Stoltz and R. H. Grubbs, Silylation of C–H bonds in aromatic heterocycles by an Earth-abundant metal catalyst, *Nature*, 2015, **518**, 80–84.

9 A. J. Smith, D. Dimitrova, J. N. Arokianathar, K. Kolodziejczak, A. Young, M. Allison, D. L. Poole, S. G. Leach, J. A. Parkinson, T. Tuttle and J. A. Murphy, New reductive rearrangement of N-arylindoles triggered by the Grubbs–Stoltz reagent Et3SiH/KOtBu, *Chem. Sci.*, 2020, **11**, 3719–3726.

10 A. J. Smith, A. Young, S. Rohrbach, E. F. O'Connor, M. Allison, H.-S. Wang, D. L. Poole, T. Tuttle and J. A. Murphy, Electron-Transfer and Hydride-Transfer Pathways in the Stoltz–Grubbs Reducing System (KOtBu/Et3SiH), *Angew. Chem., Int. Ed.*, 2017, **56**, 13747–13751.

11 W.-B. Liu, D. P. Schuman, Y.-F. Yang, A. A. Toutov, Y. Liang, H. F. T. Klare, N. Nesnas, M. Oestreich, D. G. Blackmond, S. C. Virgil, S. Banerjee, R. N. Zare, R. H. Grubbs, K. N. Houk and B. M. Stoltz, Potassium tert-Butoxide-Catalyzed Dehydrogenative C–H Silylation of Heteroaromatics: A Combined Experimental and Computational Mechanistic Study, *J. Am. Chem. Soc.*, 2017, **139**, 6867–6879.

12 J. P. Barham, G. Coulthard, K. J. Emery, E. Doni, F. Cumine, G. Nocera, M. P. John, L. E. A. Berlouis, T. McGuire, T. Tuttle and J. A. Murphy, KOtBu: A Privileged Reagent for Electron Transfer Reactions?, *J. Am. Chem. Soc.*, 2016, **138**, 7402–7410.

13 P. Asgari, Y. Hua, A. Bokka, C. Thiamsiri, W. Prasitwatcharakorn, A. Karedath, X. Chen, S. Sardar, K. Yum, G. Leem, B. S. Pierce, K. Nam, J. Gao and J. Jeon, Catalytic hydrogen atom transfer from hydrosilanes to vinylarenes for hydrosilylation and polymerization, *Nat. Catal.*, 2019, **2**, 164–173.

14 F. Palumbo, S. Rohrbach, T. Tuttle and J. A. Murphy, N-Silylation of Amines Mediated by Et3SiH/KOBu, *Helv. Chim. Acta*, 2019, **102**, e1900235.

15 S. Banerjee, Y.-F. Yang, I. D. Jenkins, Y. Liang, A. A. Toutov, W.-B. Liu, D. P. Schuman, R. H. Grubbs, B. M. Stoltz, E. H. Krenske, K. N. Houk and R. N. Zare, Ionic and Neutral Mechanisms for C–H Bond Silylation of Aromatic Heterocycles Catalyzed by Potassium tert-Butoxide, *J. Am. Chem. Soc.*, 2017, **139**, 6880–6887.

16 G.-J. Cheng, X. Zhang, L. W. Chung, L. Xu and Y.-D. Wu, Computational Organic Chemistry: Bridging Theory and Experiment in Establishing the Mechanisms of Chemical Reactions, *J. Am. Chem. Soc.*, 2015, **137**, 1706–1725.

17 S. H. Mushrif, J. J. Varghese and C. B. Krishnamurthy, Solvation dynamics and energetics of intramolecular hydride transfer reactions in biomass conversion, *Phys. Chem. Chem. Phys.*, 2015, **17**, 4961–4969.

18 G. Norjmaa, G. Ujaque and A. Lledós, Beyond Continuum Solvent Models in Computational Homogeneous Catalysis, *Top. Catal.*, 2022, **65**, 118–140.

19 J. Zhang, H. Zhang, T. Wu, Q. Wang and D. van der Spoel, Comparison of Implicit and Explicit Solvent Models for the Calculation of Solvation Free Energy in Organic Solvents, *J. Chem. Theory Comput.*, 2017, **13**, 1034–1043.

20 J.-J. Sun and J. Cheng, Solid-to-liquid phase transitions of sub-nanometer clusters enhance chemical transformation, *Nat. Commun.*, 2019, **10**, 5400.

21 J. Zeng, D. Zhang, D. Lu, P. Mo, Z. Li, Y. Chen, M. Rynik, L. a. Huang, Z. Li, S. Shi, Y. Wang, H. Ye, P. Tuo, J. Yang, Y. Ding, Y. Li, D. Tisi, Q. Zeng, H. Bao, Y. Xia, J. Huang, K. Muraoka, Y. Wang, J. Chang, F. Yuan, S. L. Bore, C. Cai, Y. Lin, B. Wang, J. Xu, J.-X. Zhu, C. Luo, Y. Zhang, R. E. A. Goodall, W. Liang, A. K. Singh, S. Yao, J. Zhang, R. Wentzcovitch, J. Han, J. Liu, W. Jia, D. M. York, W. E, R. Car, L. Zhang and H. Wang, DeePMD-kit v2: A software package for deep potential models, *J. Chem. Phys.*, 2023, **159**, 054801.

22 L. Zhang, J. Han, H. Wang, W. A. Saidi, R. Car and E. Weinan, presented in part at the *Proceedings of the 32nd International Conference on Neural Information Processing Systems*, Montréal, Canada, 2018.

23 D. J. Evans and B. L. Holian, The Nose–Hoover thermostat, *J. Chem. Phys.*, 1985, **83**, 4069–4074.

24 M. Parrinello and A. Rahman, Polymorphic transitions in single crystals: A new molecular dynamics method, *J. Appl. Phys.*, 1981, **52**, 7182–7190.

25 G. A. Tribello, M. Bonomi, D. Branduardi, C. Camilloni and G. Bussi, PLUMED 2: New feathers for an old bird, *Comput. Phys. Commun.*, 2014, **185**, 604–613.

26 A. Barducci, G. Bussi and M. Parrinello, Well-Tempered Metadynamics: A Smoothly Converging and Tunable Free-Energy Method, *Phys. Rev. Lett.*, 2008, **100**, 020603.

27 G. Bussi and A. Laio, Using metadynamics to explore complex free-energy landscapes, *Nat. Rev. Phys.*, 2020, **2**, 200–212.

28 Y. Zhang, H. Wang, W. Chen, J. Zeng, L. Zhang, H. Wang and W. E, DP-GEN: A concurrent learning platform for the generation of reliable deep learning based potential energy models, *Comput. Phys. Commun.*, 2020, **253**, 107206.

29 T. D. Kühne, M. Iannuzzi, M. Del Ben, V. V. Rybkin, P. Seewald, F. Stein, T. Laino, R. Z. Khaliullin, O. Schütt, F. Schiffmann, D. Golze, J. Wilhelm, S. Chulkov, M. H. Bani-Hashemian, V. Weber, U. Borštnik, M. Taillefumier, A. S. Jakobovits, A. Lazzaro, H. Pabst, T. Müller, R. Schade, M. Guidon, S. Andermatt, N. Holmberg, G. K. Schenter, A. Hehn, A. Bussy, F. Belleflamme, G. Tabacchi, A. Glöß, M. Lass, I. Bethune, C. J. Mundy, C. Plessl, M. Watkins, J. VandeVondele, M. Krack and J. Hutter, CP2K: An electronic structure and molecular dynamics software package - Quickstep: Efficient and accurate electronic structure calculations, *J. Chem. Phys.*, 2020, **152**, 194103.

30 J. P. Perdew, K. Burke and M. Ernzerhof, Generalized Gradient Approximation Made Simple, *Phys. Rev. Lett.*, 1996, **77**, 3865–3868.

31 C. Hartwigsen, S. Goedecker and J. Hutter, Relativistic separable dual-space Gaussian pseudopotentials from H to Rn, *Phys. Rev. B*, 1998, **58**, 3641–3662.

32 S. Goedecker, M. Teter and J. Hutter, Separable dual-space Gaussian pseudopotentials, *Phys. Rev. B*, 1996, **54**, 1703–1710.

33 S. Grimme, J. Antony, S. Ehrlich and H. Krieg, A consistent and accurate *ab initio* parametrization of density functional dispersion correction (DFT-D) for the 94 elements H-Pu, *J. Chem. Phys.*, 2010, **132**, 154104.

34 C. Kumar and S. Luber, Robust ΔSCF calculations with direct energy functional minimization methods and STEP for molecules and materials, *J. Chem. Phys.*, 2022, **156**, 154104.

35 M. Yang, L. Bonati, D. Polino and M. Parrinello, Using metadynamics to build neural network potentials for reactive events: the case of urea decomposition in water, *Catal. Today*, 2022, **387**, 143–149.

36 F. Wang, Y. Sun and J. Cheng, Switching of Redox Levels Leads to High Reductive Stability in Water-in-Salt Electrolytes, *J. Am. Chem. Soc.*, 2023, **145**, 4056–4064.

37 D. Zhang, X. Liu, X. Zhang, C. Zhang, C. Cai, H. Bi, Y. Du, X. Qin, A. Peng, J. Huang, B. Li, Y. Shan, J. Zeng, Y. Zhang, S. Liu, Y. Li, J. Chang, X. Wang, S. Zhou, J. Liu, X. Luo, Z. Wang, W. Jiang, J. Wu, Y. Yang, J. Yang, M. Yang, F.-Q. Gong, L. Zhang, M. Shi, F.-Z. Dai, D. M. York, S. Liu, T. Zhu, Z. Zhong, J. Lv, J. Cheng, W. Jia, M. Chen, G. Ke, W. E, L. Zhang and H. Wang, DPA-2: a large atomic model as a multi-task learner, *npj Comput. Mater.*, 2024, **10**, 293.

38 S. Liu, H. Yang, Y.-N. Wang, Q. Zhao, Y. Wang, R. Bai, Q. Liu and Y. Lan, Enhancing Hydride Transfer in Catalytic Hydrogenation *via* σ-Electron-Induced Polarization of Imines, *J. Am. Chem. Soc.*, 2024, **146**, 16357–16362.

39 G. Chen, D. Tian, X. Wang and H.-J. Zhang, Reductive Olefin Bicyclo[1.1.0]butane Coupling Enabled by Iron Hydride Hydrogen Atom Transfer, *ACS Catal.*, 2024, **14**, 14928–14936.

40 Y. Chen, J. Zhang, Y. Wang, H. Du, J. Xu and Z. Yang, En Route to Diastereopure Polycyclic γ-Lactones by Iridium-Catalyzed Hydride Transfer, *Chin. J. Chem.*, 2024, **42**, 3047–3055.

41 M. H. Chisholm, S. R. Drake, A. A. Naiini and W. E. Streib, Synthesis and X-ray crystal structures of the one-dimensional ribbon chains [MOBut·ButOH]∞ and the cubane species [MOBut]4 (M = K and Rb), *Polyhedron*, 1991, **10**, 337–345.

42 C. Kleeberg, Synthesis and Characterisation of [K(18-Crown-6)(OtBu)]: An Useful Reagent in Nonpolar Solvents, *Z. Anorg. Allg. Chem.*, 2011, **637**, 1790–1794.

43 Y. Feng, H. Dong and Y. Bu, Modulating electron distributions by integrating ligands with metal molecules in THF, *J. Mol. Liq.*, 2023, **391**, 123290.

44 A. I. Ojeda-Amador, A. J. Martínez-Martínez, G. M. Robertson, S. D. Robertson, A. R. Kennedy and C. T. O'Hara, Exploring the solid state and solution structural chemistry of the utility amide potassium hexamethyldisilazide (KHMDS), *Dalton Trans.*, 2017, **46**, 6392–6403.

45 C. Chuit, R. J. P. Corriu, C. Reye and J. C. Young, Reactivity of penta- and hexacoordinate silicon compounds and their role as reaction intermediates, *Chem. Rev.*, 1993, **93**, 1371–1448.

46 M. Kümper, F. F. Westermair, T. Götz, R. M. Gschwind and J. O. Bauer, Si—H Activation *via* Dynamic Permutational Isomerism: A Ligand-Directed Route to Dehydrogenative Coupling, *Angew. Chem., Int. Ed.*, 2025, **64**, e202517017.

47 P. D. Prince, M. J. Bearpark, G. S. McGrady and J. W. Steed, Hypervalent hydridosilicates: synthesis, structure and hydride bridging, *Dalton Trans.*, 2008, 271–282, DOI: 10.1039/B713427D.

48 N. Ansmann, D. Hartmann, S. Sailer, P. Erdmann, R. Maskey, M. Schorpp and L. Greb, Synthesis and Characterization of Hypercoordinated Silicon Anions: Catching Intermediates of Lewis Base Catalysis, *Angew. Chem., Int. Ed.*, 2022, **61**, e202203947.

49 R. S. Mulliken, Electronic Population Analysis on LCAO–MO Molecular Wave Functions. I, *J. Chem. Phys.*, 1955, **23**, 1833–1840.

50 E. H. Tallmadge, J. Jermaks and D. B. Collum, Structure–Reactivity Relationships in Lithiated Evans Enolates: Influence of Aggregation and Solvation on the Stereochemistry and Mechanism of Aldol Additions, *J. Am. Chem. Soc.*, 2016, **138**, 345–355.

51 R. A. Woltornist and D. B. Collum, Ketone Enolization with Sodium Hexamethyldisilazide: Solvent- and Substrate-Dependent E–Z Selectivity and Affiliated Mechanisms, *J. Am. Chem. Soc.*, 2021, **143**, 17452–17464.

52 J. Y. Yang, S. E. Smith, T. Liu, W. G. Dougherty, W. A. Hoffert, W. S. Kassel, M. R. DuBois, D. L. DuBois and R. M. Bullock, Two Pathways for Electrocatalytic Oxidation of Hydrogen by a Nickel Bis(diphosphine) Complex with Pendant Amines in the Second Coordination Sphere, *J. Am. Chem. Soc.*, 2013, **135**, 9700–9712.

53 Y. Matsubara, E. Fujita, M. D. Doherty, J. T. Muckerman and C. Creutz, Thermodynamic and Kinetic Hydricity of Ruthenium(II) Hydride Complexes, *J. Am. Chem. Soc.*, 2012, **134**, 15743–15757.

54 D. J. Anick and K. Leung, Transition states for hydride-water (H−)(H2O)n clusters, n=2–6, 20, *J. Mol. Struct.*, 2009, **916**, 61–71.

55 Y. Kim, Y. Park and S. Chang, Delineating Physical Organic Parameters in Site-Selective C–H Functionalization of Indoles, *ACS Cent. Sci.*, 2018, **4**, 768–775.

56 V. A. Roytman and D. A. Singleton, Solvation Dynamics and the Nature of Reaction Barriers and Ion-Pair Intermediates in Carbocation Reactions, *J. Am. Chem. Soc.*, 2020, **142**, 12865–12877.

57 Y. Basdogan and J. A. Keith, A paramedic treatment for modeling explicitly solvated chemical reaction mechanisms, *Chem. Sci.*, 2018, **9**, 5341–5346.

58 M. S. Dresselhaus and G. Dresselhaus, Intercalation compounds of graphite, *Adv. Phys.*, 1981, **30**, 139–326.

59 E. von Grotthuss, S. E. Prey, M. Bolte, H.-W. Lerner and M. Wagner, Dual Role of Doubly Reduced Arylboranes as

Dihydrogen- and Hydride-Transfer Catalysts, *J. Am. Chem. Soc.*, 2019, **141**, 6082–6091.

60 J. C. Wedal, L. M. Anderson-Sanchez, M. T. Dumas, C. A. Gould, M. J. Beltrán-Leiva, C. Celis-Barros, D. Páez-Hernández, J. W. Ziller, J. R. Long and W. J. Evans, Synthesis and Crystallographic Characterization of a Reduced Bimetallic Yttrium ansa-Metallocene Hydride Complex, [K(crypt)][(μ-CpAn)Y(μ-H)]2 (CpAn = Me2Si [C5H3(SiMe3)-3]2), with a 3.4 Å Yttrium–Yttrium Distance, *J. Am. Chem. Soc.*, 2023, **145**, 10730–10742.

61 Z. Feng and R. Kinjo, Edge-condensation to access a crystalline planar icosagen cation with σ-aromaticity, *Nat. Commun.*, 2025, **16**, 9982.

62 C. B. van Beek, N. P. van Leest, M. Lutz, S. D. de Vos, R. J. M. Klein Gebbink, B. de Bruin and D. L. J. Broere, Combining metal–metal cooperativity, metal–ligand cooperativity and chemical non-innocence in diiron carbonyl complexes, *Chem. Sci.*, 2022, **13**, 2094–2104.

63 D. A. Papaconstantopoulos, in *Band Structure of Cubic Hydrides*, ed. D. A. Papaconstantopoulos, Springer International Publishing, Cham, 2023, pp. 37–74, DOI: 10.1007/978-3-031-06878-2_3.

64 Z. Grobelny, J. Jurek-Suliga and S. Golba, Ring-opening polymerization of monosubstituted oxiranes in the presence of potassium hydride: determination of initiation course and structure of macromolecules by MALDI-TOF mass spectrometry, *J. Polym. Res.*, 2019, **26**, 274.

65 D. F. Taber and C. G. Nelson, Potassium Hydride in Paraffin: A Useful Base for Organic Synthesis, *J. Org. Chem.*, 2006, **71**, 8973–8974.